Probing Flat Band Physics in Spin Ice Systems via Polarized Neutron Scattering

K. T. K. Chung,[1,*] J. S. K. Goh,[1,2] A. Mukherjee,[1,4] W. Jin,[1] D. Lozano-Gómez,[1] and M. J. P. Gingras[1,3]
[1]Department of Physics and Astronomy, University of Waterloo, Ontario N2L 3G1, Canada
[2]Division of Physics and Applied Physics, School of Physical and Mathematical Sciences, Nanyang Technological University, 21 Nanyang Link 637371, Singapore
[3]CIFAR, MaRS Centre, West Tower 661 University Avenue, Suite 505, Toronto, Ontario M5G 1M1, Canada
[4]Institute of Physics, University of Amsterdam, Science Park 904, 1098 XH Amsterdam, The Netherlands

(Received 1 August 2021; accepted 27 January 2022; published 10 March 2022)

In this Letter, we illustrate how polarized neutron scattering can be used to isolate the spin-spin correlations of modes forming flat bands in a frustrated magnetic system hosting a classical spin liquid phase. In particular, we explain why the nearest-neighbor spin ice model, whose interaction matrix has two flat bands, produces a dispersionless (i.e., "flat") response in the non-spin-flip (NSF) polarized neutron scattering channel and demonstrate that NSF scattering is a highly sensitive probe of correlations induced by weak perturbations that lift the flat band degeneracy. We use this to explain the experimentally measured dispersive (i.e., nonflat) NSF channel of the dipolar spin ice compound $Ho_2Ti_2O_7$.

DOI: 10.1103/PhysRevLett.128.107201

Momentum-independent bands in electronic and magnetic systems are indicative of spatially localized excitations of the pertinent degrees of freedom. Systems with such flat bands boast a huge sensitivity to perturbations, often giving rise to exotic strongly correlated states of matter [1–3]. Highly frustrated magnets, such as antiferromagnetically coupled spins on kagome and pyrochlore lattices, have proven to be a seemingly inexhaustible gold mine to explore flat bands and their consequential physics, with spin ice (SI) systems [4,5] providing a particularly fruitful setting to do so.

Momentum-resolved probes [6–10] are the most direct methods to study flat bands experimentally, with neutron scattering being the method of choice for magnetic systems [9,10]. The neutron moment (spin) is sensitive to two of the three components of the local magnetic field produced by the material's magnetic moments. Neutron spin polarization analysis separates the moments' correlations into two channels, referred to as the spin-flip and non-spin-flip (SF and NSF, respectively) [11,12].

The flat bands of classical SI [13,14] give rise to a low-temperature collective paramagnetic Coulomb phase [15–17] whose emergent gauge structure is signaled in reciprocal space by "pinch points" in the neutron cross sections [15–17]. In SI, pinch points were first [18] experimentally investigated in $Ho_2Ti_2O_7$ [19–21] using polarized neutron scattering [18]. In this compound, the SF channel displays pinch points in the (hhl) scattering plane, reflecting singularities in the spin-spin correlations, which are understood by mapping the spins to a divergence-free vector field $\boldsymbol{B}$ [15–17,22]. Conversely, NSF scattering in $Ho_2Ti_2O_7$ [18] exhibits only broad diffuse features in (hhl) and has received minimal attention.

Interestingly, it has been noted several times [18,23–27] that nearest-neighbor spin ice (NNSI), a foundational minimal model [4,19,28] hosting a Coulomb phase and thus pinch points [15–17], displays a momentum-independent (i.e., flat) NSF (hhl) scattering intensity. Given that the NNSI model has been extensively studied and is well understood [5,15–17,29–31], it is surprising that this fact has not been scrutinized in any detail. This raises the questions addressed in this Letter: how is the flat NSF intensity of NNSI related to its flat bands [13,14], what is the underlying physics of this relationship, and how does the NSF acquire dispersion when interactions beyond nearest neighbor are introduced?

Using Monte Carlo simulations and a large-N approximation, we confirm that NNSI and an extended spin ice (ESI) model [32,33] exhibit a flat NSF at *all* temperatures, but with a magnitude rising monotonically as temperature decreases [see Figs. 1(c)–1(e)]. The NSF intensity in the (hhl) plane is shown to directly probe fluctuations of modes constructed from the flat band eigenvectors of the interaction matrix. We show how dispersion in the NSF, which develops when moving away from the ESI model, is a sensitive indicator of the dispersion acquired by the originally flat bands and explain how a dispersive NSF arises in $Ho_2Ti_2O_7$ [18,34].

Model and methods.—We consider a pyrochlore lattice consisting of L^3 face-centered-cubic (fcc) unit cells with four sites per cell [Figs. 1(a) and 1(b)] and periodic boundaries (see the Supplemental Material [35] for conventions). Each site i of the pyrochlore lattice hosts a classical Ising spin [42,43], $s_i = \pm 1$, whose magnetic moments $\boldsymbol{\mu}_i \propto s_i \hat{\boldsymbol{z}}_i$ are constrained along the local cubic $[111]$ axes $\hat{\boldsymbol{z}}_i$. We consider a spin Hamiltonian with

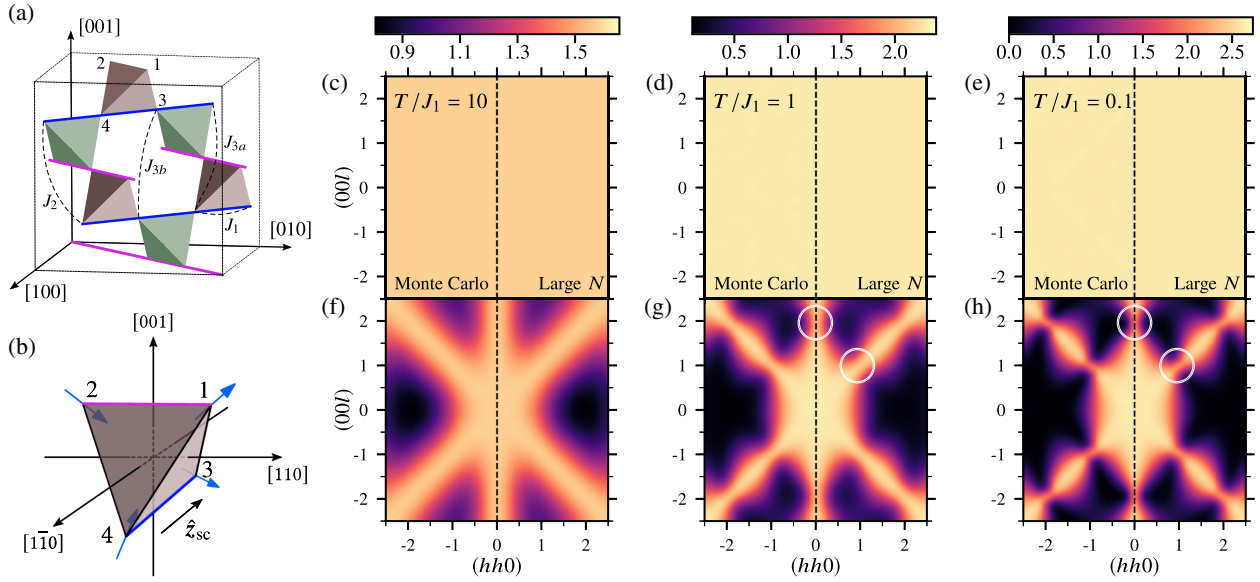

FIG. 1. (a) The pyrochlore lattice with its four labeled sublattices and couplings J_n up to third neighbor. α chains along $[\bar{1}10]$ discussed in the main text are highlighted in blue. (b) Two-in–two-out ice rule obeying configuration of Ising spins on a tetrahedron. (c)–(e) NSF and (f)–(h) SF for NNSI in the (hhl) plane, with pinch points indicated by white circles. The left (right) half of each panel shows the Monte Carlo (large-N) results.

interactions between first, second, and third (class a, but not class b [32,44,45]) nearest neighbors [see Fig. 1(a)],

$$H = J_1 \sum_{\langle i,j \rangle} s_i s_j + J_2 \sum_{\langle\langle i,j \rangle\rangle} s_i s_j + J_{3a} \sum_{\langle\langle\langle i,j \rangle\rangle\rangle_a} s_i s_j, \qquad (1)$$

with $J_1 > 0$. Restricting to the line in parameter space $J_2 = J_{3a} \equiv J'$, one obtains the ESI model [32,33], for which an extensive number of spin configurations obeying the two-in–two-out "ice rules" [illustrated in Fig. 1(b)] are energetically degenerate [4,15–17,19,46]. In the range $-0.5 < J'/J_1 < 0.25$ (including NNSI at $J' = 0$), these configurations are the ground states [32,33], and we refer to this restricted range as "the ESI line."

In polarized neutron scattering (sc) experiments with incident neutron polarization axis $\hat{z}_{sc}$, one defines an orthonormal basis for each scattering wave vector $\boldsymbol{q} \perp \hat{z}_{sc}$, with $\hat{x}_{sc} \equiv \hat{q}$ and $\hat{y}_{sc} \equiv \hat{z}_{sc} \times \hat{x}_{sc}$ [35]. The scattered neutron moment is only sensitive to the $\hat{y}_{sc}$ and $\hat{z}_{sc}$ components of the magnetic moments $\boldsymbol{\mu}_i$, whose correlations are separated by filtering the scattered beam by neutron spin polarization [11,12]. This gives energy-integrated SF and NSF cross sections [18,34,47], respectively proportional to the following two structure factors [35]:

$$\sigma_{SF}(\boldsymbol{q}) = \sum_{\mu,\nu} (\hat{z}_\mu \cdot \hat{y}_{sc}) \langle s^*_\mu(\boldsymbol{q}) s_\nu(\boldsymbol{q}) \rangle (\hat{z}_\nu \cdot \hat{y}_{sc}), \qquad (2)$$

$$\sigma_{NSF}(\boldsymbol{q}) = \sum_{\mu,\nu} (\hat{z}_\mu \cdot \hat{z}_{sc}) \langle s^*_\mu(\boldsymbol{q}) s_\nu(\boldsymbol{q}) \rangle (\hat{z}_\nu \cdot \hat{z}_{sc}). \qquad (3)$$

Here, μ and ν label the four fcc sublattices [Figs. 1(a) and 1(b)], and $s_\mu(\boldsymbol{q}) \equiv L^{-3/2} \sum_{i \in \mu} s_i e^{-i\boldsymbol{q}\cdot\boldsymbol{r}_i}$ are the Fourier-transformed Ising variables (see the Supplemental Material [35] for conventions). Our focus is the experimentally preferred (hhl) plane [9,18,34,47] with $\hat{z}_{sc} \equiv [\bar{1}10]$ [see Fig. 1(b)].

To calculate the spin-spin correlations in Eqs. (2) and (3), we employ the large-N approximation [22,48] (see Supplemental Material [35] for details), previously successfully used to expose many key aspects of SI physics [29,49–51]. We write Eq. (1) as $H = \frac{1}{2} \sum_{ij} s_i V_{ij} s_j$, where V is the interaction matrix, with V_{ij} the coupling between sites i and j, and $V_{ii} \equiv \bar{\epsilon}$ chosen to shift the minimum eigenvalue of V to zero [22,35]. The large-N correlation matrix $\mathcal{G}_{ij} \equiv \langle s_i s_j \rangle = [\lambda \mathbb{1} + \beta V]^{-1}_{ij}$ is 4×4 block diagonal in $\boldsymbol{q}$ space [29],

$$\mathcal{G}_{\mu\nu}(\boldsymbol{q}) \equiv \langle s^*_\mu(\boldsymbol{q}) s_\nu(\boldsymbol{q}) \rangle = [\lambda \mathbb{1}_{4\times4} + \beta V(\boldsymbol{q})]^{-1}_{\mu\nu}. \qquad (4)$$

Here, $\beta = 1/T$ with T the temperature ($k_B \equiv 1$), and λ is a positive temperature-dependent Lagrange multiplier determined self-consistently [22,29,51] by the saddle-point condition $\mathrm{Tr}\,\mathcal{G} \equiv \sum_i \langle s_i^2 \rangle = 4L^3$ (the number of spins).

Results.—Starting with NNSI ($J' = 0$), σ_{SF} [Figs. 1(f)–1(h)] displays a distinct scattering pattern in (hhl), with pinch points (white circles) developing for $T/J_1 \lesssim 1$, signaling the onset of the Coulomb phase. In contrast, σ_{NSF} [Figs. 1(c)–1(e)] is $\boldsymbol{q}$ independent at all temperatures, with intensity rising monotonically as temperature decreases. Analogous results are obtained for models on

the ESI line [35,52]. In all cases, a flat $\sigma_{\rm NSF}$ is only observed for $\boldsymbol{q} \in (hhl)$ and symmetry-equivalent planes—cf. the nonflat NNSI $\sigma_{\rm NSF}$ for $\boldsymbol{q} \in (h0l)$ in the Supplemental Material [35].

To investigate the origin of this flatness, let $\boldsymbol{\Omega}$ be a four-component vector with components $\Omega_\mu \equiv (\hat{z}_{\rm sc} \cdot \hat{z}_\mu)$ in the sublattice basis and normalized components denoted $\hat{\Omega}_\mu \equiv \Omega_\mu/|\boldsymbol{\Omega}|$, with which we rewrite Eq. (3) as

$$\sigma_{\rm NSF}(\boldsymbol{q}) = |\boldsymbol{\Omega}|^2 \langle |\hat{\Omega}_\mu s_\mu(\boldsymbol{q})|^2 \rangle, \tag{5}$$

with henceforth, implied summation over repeated index μ in $\hat{\Omega}_\mu s_\mu(q)$. We refer to the normalized linear combination of spin variables $\hat{\Omega}_\mu s_\mu(\boldsymbol{q})$ as a "mode" (one mode for each $\boldsymbol{q}$) and interpret $\langle |\hat{\Omega}_\mu s_\mu(\boldsymbol{q})|^2 \rangle$ as its thermal occupation value (TOV). Crucially, when $\hat{z}_{\rm sc} \| [\bar{1}10]$, the Ising moments on sublattices 1 and 2 lie orthogonal to $\hat{z}_{\rm sc}$ [see Fig. 1(b)] so that $\boldsymbol{\Omega} = \sqrt{2/3}(0,0,1,-1)$ and $|\boldsymbol{\Omega}|^2 = 4/3$; only spins on sublattices 3 and 4 contribute to NSF scattering in the (hhl) plane.

To evaluate $\sigma_{\rm NSF}$ in Eq. (5), we begin with a spectral decomposition of V, $V_{ij} = \sum_{\boldsymbol{q},n} \epsilon_n(\boldsymbol{q}) [\hat{\psi}_n(\boldsymbol{q})]_i [\hat{\psi}_n(\boldsymbol{q})]_j^*$ [13,53]. The normalized eigenvectors $\hat{\boldsymbol{\psi}}_n(\boldsymbol{q})$ $(n = 1, \ldots, 4)$ define the "normal modes" $\tilde{s}_n(\boldsymbol{q}) \equiv \sum_i [\hat{\psi}_n(\boldsymbol{q})]_i s_i$, with sum over sites i. The corresponding eigenvalues $\epsilon_n(\boldsymbol{q}) \geq 0$ are the normal mode energies, forming four bands indexed by n, with the Hamiltonian now written as $H = \frac{1}{2} \sum_{\boldsymbol{q},n} \epsilon_n(\boldsymbol{q}) |\tilde{s}_n(\boldsymbol{q})|^2$. The correlation matrix $\mathcal{G}$ [Eq. (4)] shares the eigenvectors of V and its eigenvalues are precisely the normal mode TOVs, $\langle |\tilde{s}_n(\boldsymbol{q})|^2 \rangle = [\lambda + \beta \epsilon_n(\boldsymbol{q})]^{-1}$.

The interaction matrix for NNSI is $V_{\rm NNSI} \equiv J_1(A + 2\mathbb{1})$ and, for ESI, $V_{\rm ESI} \equiv V_{\rm NNSI} + J'(A^2 - 2A - 8\mathbb{1})$ [3]. Here, A is the $4L^3 \times 4L^3$ pyrochlore nearest-neighbor adjacency matrix encoding the connectivity of the lattice, which is block diagonal in $\boldsymbol{q}$ space, with each 4×4 block denoted $A(\boldsymbol{q})$. Importantly, A has two flat band, $\epsilon_n(\boldsymbol{q}) = -2$, at the bottom of its spectrum due to the geometric frustration of this lattice. Since $V_{\rm NNSI}$ and $V_{\rm ESI}$ are polynomials of A, they share its eigenvectors and inherit zero-energy flat bands [3] and positive-energy dispersive bands. Importantly, $\hat{\boldsymbol{\Omega}}$ in Eq. (5) is a flat band eigenvector of $A(\boldsymbol{q})$ for all $\boldsymbol{q} \in (hhl)$ [35] and, consequently, also of $V_{\rm NNSI}(\boldsymbol{q})$ and $V_{\rm ESI}(\boldsymbol{q})$. From this, it follows that the aforementioned (hhl) modes $\hat{\Omega}_\mu s_\mu(\boldsymbol{q})$ probed by NSF scattering are in fact *flat band* normal modes of $V_{\rm NNSI}$ and $V_{\rm ESI}$ with $\epsilon_n(\boldsymbol{q}) = 0$, whose TOVs are $\langle |\hat{\Omega}_\mu s_\mu(\boldsymbol{q})|^2 \rangle = \lambda^{-1}$. Therefore, Eq. (5) yields

$$\sigma_{\rm NSF}(\boldsymbol{q}) = \frac{4}{3\lambda}. \tag{6}$$

Thus, the (hhl) NSF is $\boldsymbol{q}$ independent, increasing monotonically from $4/3$ in the high-T paramagnetic phase (TOV of all modes equal to $1 \Rightarrow \lambda = 1$) to $8/3$ in the low-T Coulomb phase (TOV of dispersive band modes equal to 0 and TOV of flat band modes equal to $2 \Rightarrow \lambda = 1/2$) [35] as seen in Figs. 1(c)–1(e).

Coulomb phase interpretation.—We established above that, irrespective of the V_{ij} considered, $\sigma_{\rm NSF}$ probes for each $\boldsymbol{q} \in (hhl)$ a mode $\hat{\Omega}_\mu s_\mu(\boldsymbol{q})$ constructed from the components of the flat band eigenvector $\hat{\boldsymbol{\Omega}}$ of the 4×4 $A(\boldsymbol{q})$. All of the (hhl) modes $\hat{\Omega}_\mu s_\mu(\boldsymbol{q})$ are energetically degenerate for $V_{\rm NNSI}$ and $V_{\rm ESI}$, resulting in a flat NSF. Given that the physics of NNSI and ESI is controlled entirely by the spectral properties of A, it will prove useful to adopt a terminology differentiating between modes constructed from the dispersive band eigenvectors of A and those constructed from the flat band eigenvectors. To set up this terminology, we first focus on the long-wavelength limit describing the coarse-grained Coulomb phase physics of $V_{\rm NNSI}$ and $V_{\rm ESI}$. In this limit, the pertinent normal modes of these two V's are obtained by an orthonormal change of basis [15,22],

$$Q(\boldsymbol{q}) \equiv \frac{1}{2} \sum_\mu s_\mu(\boldsymbol{q}), \qquad \boldsymbol{B}(\boldsymbol{q}) \equiv \sqrt{\frac{3}{4}} \sum_\mu s_\mu(\boldsymbol{q}) \hat{z}_\mu. \tag{7}$$

In direct space, Q and $\boldsymbol{B}$ are, respectively, akin to a charge density and a three-component vector field. The long-wavelength dispersive band modes are $Q(\boldsymbol{q})$ and $\hat{\boldsymbol{q}} \cdot \boldsymbol{B}(\boldsymbol{q})$, which are thermally depopulated at low temperature [22]. The long-wavelength flat band modes are the two remaining components of $\boldsymbol{B}(\boldsymbol{q})$, which lie in the plane orthogonal to $\hat{\boldsymbol{q}}$ (spanned by $\hat{\boldsymbol{y}}_{\rm sc}$ and $\hat{z}_{\rm sc}$). In a gauge theory like electromagnetism, the dispersive pair $\{Q(\boldsymbol{q}), \hat{\boldsymbol{q}} \cdot \boldsymbol{B}(\boldsymbol{q})\}$ would commonly be referred to as "longitudinal" modes and the flat pair $\{\hat{\boldsymbol{y}}_{\rm sc} \cdot \boldsymbol{B}(\boldsymbol{q}), \hat{z}_{\rm sc} \cdot \boldsymbol{B}(\boldsymbol{q})\}$ as "transverse" modes.

We now extend this terminology to arbitrary $\boldsymbol{q}$, where longitudinal modes are those constructed from the dispersive band eigenvectors of A, while transverse modes are those constructed from its flat band eigenvectors of A. Expressed in this basis, $\sigma_{\rm SF}$ and $\sigma_{\rm NSF}$ take simple forms,

$$\sigma_{\rm SF} = \frac{4}{3} \langle |\boldsymbol{B}(\boldsymbol{q}) \cdot \hat{\boldsymbol{y}}_{\rm sc}|^2 \rangle, \qquad \sigma_{\rm NSF} = \frac{4}{3} \langle |\boldsymbol{B}(\boldsymbol{q}) \cdot \hat{z}_{\rm sc}|^2 \rangle. \tag{8}$$

The modes whose TOVs appear in Eq. (8) are both transverse modes at *long* wavelength, which is reflected in the equal intensity of $\sigma_{\rm SF}$ and $\sigma_{\rm NSF}$ seen in Fig. 1 for small $\boldsymbol{q}$. However, for *larger* wave vectors, the SF intensity drops to zero at low temperature, indicating that $\boldsymbol{B}(\boldsymbol{q}) \cdot \hat{\boldsymbol{y}}_{\rm sc}$ is a longitudinal mode at these wave vectors. The NSF is flat throughout (hhl) because $\hat{\Omega}_\mu s_\mu(\boldsymbol{q}) \equiv \boldsymbol{B}(\boldsymbol{q}) \cdot \hat{z}_{\rm sc}$ [appearing in Eqs. (5) and (8), respectively] is a transverse mode for *all* $\boldsymbol{q}$ in this plane since $\hat{\boldsymbol{\Omega}}$ is a flat band eigenvector of $A(\boldsymbol{q})$. The lesson is that, while the SF probes *both* transverse and longitudinal modes, resulting in

pinch points, the (hhl) NSF probes *solely* transverse modes.

In the aforementioned long-wavelength theory of NNSI [15,16,22] built from Q and $\boldsymbol{B}$, the physics is controlled by λ and a screening length ξ [16] (equivalently, the charge density), which controls the width of the pinch points [16]. Since the NSF is blind to the longitudinal modes [ξ does not appear in Eq. (6)] a calibrated measurement of the temperature dependence of σ_{NSF} could afford a direct experimental determination of $\lambda(T)$ that characterizes the long-wavelength theory.

Chain correlations.—We now turn to the direct-space interpretation of the (hhl) modes $\hat{\mathbf{\Omega}}_\mu s_\mu(\boldsymbol{q})$ probed by the NSF. First, note that sublattices 3 and 4 lie on L^2 "α chains" running along $[\bar{1}10]$ [21,54,55] [Fig. 1(a) blue lines], which form a 2D isosceles triangular lattice perpendicular to $[\bar{1}10]$ [54–57]. We define an α chain's polarization $\mathsf{P}_\alpha \equiv L^{-1/2}(\sum_{i\in\alpha} s_i\hat{\boldsymbol{z}}_i)\cdot\hat{\boldsymbol{z}}_{\mathrm{sc}}$ and, for each $\boldsymbol{q}\in(hhl)$, its Fourier transform $\mathsf{P}(\boldsymbol{q}) \equiv L^{-1}\sum_\alpha \mathsf{P}_\alpha e^{-i\boldsymbol{q}\cdot\boldsymbol{R}_\alpha}$, where $\boldsymbol{R}_\alpha$ are the α-chain coordinates in the $[hhl]$ plane. One obtains [35]

$$\sigma_{\mathrm{NSF}}(\boldsymbol{q}) = \langle|\mathsf{P}(\boldsymbol{q})|^2\rangle = \frac{1}{L^2}\sum_{\alpha,\alpha'}\langle\mathsf{P}_\alpha\mathsf{P}_{\alpha'}\rangle e^{-i\boldsymbol{q}\cdot(\boldsymbol{R}_{\alpha'}-\boldsymbol{R}_\alpha)}, \quad (9)$$

i.e., $\sigma_{\mathrm{NSF}}(\boldsymbol{q})$ is the Fourier transform of the chain-chain correlation function $\langle\mathsf{P}_\alpha\mathsf{P}_{\alpha'}\rangle$. Comparing Eq. (9) with Eqs. (5) and (8), we see that the transverse mode $\hat{\mathbf{\Omega}}_\mu s_\mu(\boldsymbol{q})$ at a given $\boldsymbol{q}$ probed by $\sigma_{\mathrm{NSF}}(\boldsymbol{q})$ is the Fourier-transformed α-chain polarization $\hat{\mathbf{\Omega}}_\mu s_\mu(\boldsymbol{q}) = \sqrt{3/4}\,\mathsf{P}(\boldsymbol{q})$. A geometrical interpretation of the (hhl) NSF thus follows: trivially, sublattices 1 and 2 do not contribute because their Ising moments lie perpendicular to the α chains along which the neutrons are polarized; thus the NSF isolates the spin correlations of sublattices 3 and 4. These "3–4" chains are the support of flat band eigenvectors of A whose direct-space components alternate in sign along a given chain α and are zero on all other sites [58]. This is the geometrical origin of why $\hat{\mathbf{\Omega}}\propto(0,0,1,-1)$ is a flat band eigenvector of $A(\boldsymbol{q})$ for all $\boldsymbol{q}\in(hhl)$ (see the Supplemental Material [35]). The $\boldsymbol{q}$-independent NSF on the ESI line [Eq. (6)] indicates that $\langle\mathsf{P}_\alpha\mathsf{P}_{\alpha'}\rangle = (4/3\lambda)\delta_{\alpha\alpha'}$; the α chains are uncorrelated from each other at all temperatures, with the flat σ_{NSF} tracking the *intrachain* correlations, $\langle\mathsf{P}_\alpha^2\rangle = (4/3\lambda)$. It would be interesting to investigate how this last result arises order-by-order in an approximation-free direct-space high-temperature expansion [59] of the original SI and ESI models.

σ_{NSF} *off the ESI line.*—Contrasting with the previous discussion, a dispersive σ_{NSF} implies nontrivial *interchain* correlations, which we now consider. Together, Eqs. (3)–(5) give

$$\sigma_{\mathrm{NSF}}(\boldsymbol{q}) = |\mathbf{\Omega}|^2\hat{\mathbf{\Omega}}_\mu\mathcal{G}_{\mu\nu}(\boldsymbol{q})\hat{\mathbf{\Omega}}_\nu, \quad (10)$$

which yields $\sigma_{\mathrm{NSF}} = \frac{4}{3}[\mathcal{G}_{33}(\boldsymbol{q}) - \mathcal{G}_{34}(\boldsymbol{q})]$. In Fig. 2, we show line cuts (solid lines) of $\mathcal{G}_{33}(\boldsymbol{q})$, $\mathcal{G}_{34}(\boldsymbol{q})$, and $\sigma_{\mathrm{NSF}}(\boldsymbol{q})$ along $(hh2)$ for four (J_2, J_{3a}) parameter choices at $T/J_1 = 0.1$. The NNSI case is shown in Fig. 2(a), while Fig. 2(b) corresponds to a point on the $J_2 = J_{3a}$ ESI line, both of which have flat bands and thus exhibit a flat σ_{NSF}. Conversely, Figs. 2(c) and 2(d) illustrate that, for slight perturbations off the ESI line weakly lifting the flat band degeneracy, σ_{NSF} departs significantly from flatness [35], indicating the development of interchain correlations $\langle\mathsf{P}_\alpha\mathsf{P}_{\alpha'}\rangle$. This demonstrates that the NSF provides a sensitive probe of perturbations that lift the original flat band degeneracy and make the transverse modes dispersive.

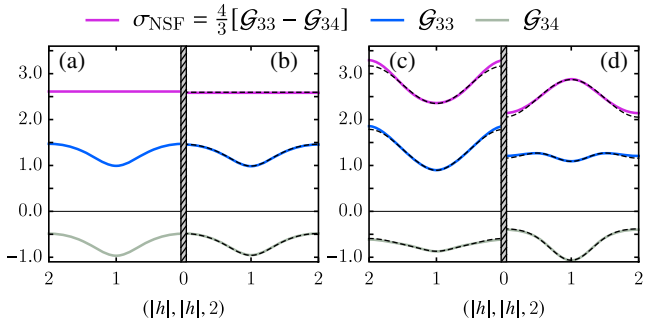

FIG. 2. Line cuts along $(hh2)$ of the $\mathcal{G}_{33}(\boldsymbol{q})$ and $\mathcal{G}_{34}(\boldsymbol{q})$ sublattice correlations, as well as $\sigma_{\mathrm{NSF}}(\boldsymbol{q})$, for $T/J_1 = 0.1$, with $(J_2/J_1, J_{3a}/J_1) =$ (a) (0, 0), (b) (0.1, 0.1), (c) $(0.001, -0.001)$, and (d) $(-0.001, 0.001)$. Solid lines show the numerically exact values from Eq. (4), whereas dashed lines show the first-order perturbative calculation.

To expose how σ_{NSF} develops dispersion, we consider perturbations V_p away from NNSI, $V = V_{\mathrm{NNSI}} + V_p$, where V_p is a linear combination of further-neighbor interaction matrices with energy scale much smaller than J_1. From Eq. (4), expanding $\lambda \equiv \lambda_0 + \lambda_p$, $\mathcal{G}$ satisfies $\mathcal{G}^{-1} = \mathcal{G}_0^{-1} + \Sigma$, where $\mathcal{G}_0 \equiv [\lambda_0\mathbb{1} + \beta V_{\mathrm{NNSI}}]^{-1}$ is the unperturbed correlation matrix and $\Sigma \equiv [\lambda_p\mathbb{1} + \beta V_p]$ contains the perturbing terms, yielding an expansion $\mathcal{G} = \mathcal{G}_0 - \mathcal{G}_0\Sigma\mathcal{G}_0 + \cdots$ (see the Supplemental Material [35] for details).

At low temperature, $\mathcal{G}_0$ is proportional to the projector onto the flat bands of V_{NNSI} [15], making $\mathcal{G}_0\Sigma\mathcal{G}_0$ the projection of Σ into the transverse mode subspace. Since $\hat{\mathbf{\Omega}}$ is an eigenvector of $\mathcal{G}_0(\boldsymbol{q})$ with eigenvalue λ_0^{-1}, Eq. (10) yields to first order

$$\sigma_{\mathrm{NSF}}(\boldsymbol{q}) \approx \frac{4}{3\lambda_0}\left(1 - \frac{1}{\lambda_0}\hat{\mathbf{\Omega}}_\mu\Sigma_{\mu\nu}(\boldsymbol{q})\hat{\mathbf{\Omega}}_\nu\right). \quad (11)$$

The first-order correction yields a dispersive contribution to the NSF, reflecting how V_p causes the (hhl) transverse modes $\hat{\mathbf{\Omega}}_\mu s_\mu(\boldsymbol{q})$ to become dispersive. Figures 2(b)–2(d) compares Eq. (11) (dashed lines) with the exact calculation (solid lines), demonstrating that Eq. (11) accurately captures the departure from flatness when perturbing off the ESI line.

NSF of dipolar spin ice.—A natural physically relevant setting to explore how σ_{NSF} acquires dispersion is to consider a dipolar spin ice (DSI) model in which the

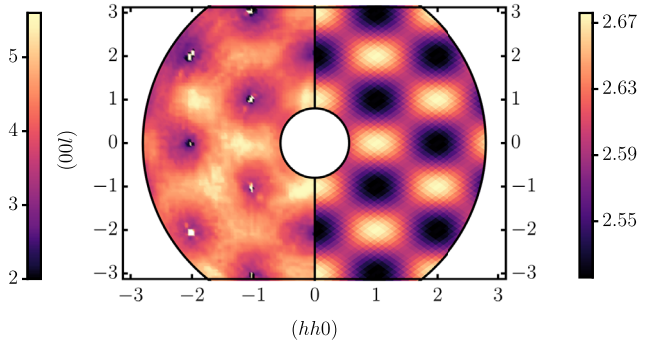

FIG. 3. Left: the NSF channel intensity (in arbitrary units) measured via polarized neutron scattering in $Ho_2Ti_2O_7$. Right: σ_{NSF} calculated via (12) taking $J_{\mathrm{dip}}/J_1 = 0.03$ and $T/J_1 = 0.1$. Figure adapted from panel B of Fig. 2 of Ref. [18], with permission from the American Association for the Advancement of Science.

long-range dipolar interactions added to the NNSI model are treated perturbatively. This is directly relevant to the weak-moment non-Kramers Pr^{3+}-based $[Pr_2(Sn, Hf, Zr)_2O_7]$ quantum SI materials [31,60,61] and is also pertinent to $Ho_2Ti_2O_7$ [19–21] and $Dy_2Ti_2O_7$ [62,63] DSI compounds. We take $V_p = J_{\mathrm{dip}}\mathcal{D}$, where $\mathcal{D}$ is the dimensionless form of the dipolar interaction matrix [35], which we decompose using the "projective equivalence" of Ref. [14], $\mathcal{D} = c\mathcal{P} + \Delta$. Here, c is a proportionality constant and $\mathcal{P}$ is the projector into the *dispersive* band eigenspace of A (the longitudinal mode subspace) containing the long-range $1/R^3$ portion of the interaction. Δ contains small short-range corrections decaying as $1/R^5$ [14,35]. The key observation is that $\mathcal{P}_{\mu\nu}(\boldsymbol{q})\hat{\Omega}_\nu = 0$ because $\hat{\boldsymbol{\Omega}}$ is a flat band eigenvector for $\boldsymbol{q} \in (hhl)$. Therefore, the leading-order dispersive correction to the originally flat $\sigma_{\mathrm{NSF}}(\boldsymbol{q})$ in Eq. (11) is *entirely* due to the weak short-range corrections contained in Δ_{ij}, giving

$$\sigma_{\mathrm{NSF}}(\boldsymbol{q}) \approx \frac{4}{3\lambda_0}\left(1 - \frac{1}{\lambda_0}\hat{\Omega}_\mu[\lambda_p\delta_{\mu\nu} + \beta J_{\mathrm{dip}}\Delta_{\mu\nu}(\boldsymbol{q})]\hat{\Omega}_\nu\right). \quad (12)$$

We therefore conclude that the (hhl) NSF of this weak-moment DSI model is *insensitive* to the long-range portion of the interaction contained in $\mathcal{P}$, which encodes the $1/R$ Coulomb interaction between monopoles [64]. It is, instead, sensitive to the dispersion of the transverse modes induced by the weak lifting of the flat band degeneracy via the interactions contained in Δ_{ij} [14]. To illustrate this, we show in Fig. 3 the experimental NSF of $Ho_2Ti_2O_7$ [18] compared to $\sigma_{\mathrm{NSF}}(\boldsymbol{q})$ computed using Eq. (12) with $\beta J_{\mathrm{dip}} = 0.3$ (see the Supplemental Material [35] for details). The qualitative agreement between the perturbative and experimental results is reasonable because the dispersion in the flat bands of DSI is very small relative to the dipolar interaction scale J_{dip}—the phenomenon of "self-screening" [13,14].

Conclusion.—In this Letter, we considered the problem of polarized neutron scattering of Ising magnetic moments on the pyrochlore lattice. We found that the non-spin-flip neutron scattering cross section in the (hhl) plane directly probes fluctuations of the flat band modes (i.e. transverse modes) of the spin-spin interaction matrix. This explains the origin of the long-noted momentum-independent NSF of classical extended spin ice systems, in particular, nearest-neighbor spin ice [18,23–27]. Furthermore, we showed that the NSF channel serves as a sensitive probe of perturbations that lift the flat band degeneracy. Crucially, our results only rely on the moments being Ising, resulting in the isolation of the α chains and thus the NSF probing solely transverse modes, suggesting a broad range of applicability in geometrically frustrated Ising magnets.

Our Letter illustrates that an analysis of σ_{NSF} could prove a fruitful approach to parametrize interactions beyond nearest neighbor [62,63], quantum fluctuations [25], and lattice strain [65] in spin ice–like systems. In relation to the former, as indicated in Figs. 2(c) and 2(d), the shape of the NSF dispersion reflects whether one is above or below the ESI line, i.e., whether $J_2 > J_{3a}$ or $J_2 < J_{3a}$ [35]. Investigation of the NSF in diluted [34,66] and stuffed spin ice [67] would also be interesting. Another intriguing line of inquiry is to characterize the development of nonflat NSF features arising from quantum fluctuations in the XXZ model of quantum spin ice [68], as observed in quantum Monte Carlo simulations [25] and attributed to the emergent photon of the deconfined U(1) gauge theory description of the model [31,69]. It would be worthwhile to make use of the understanding reached in the present work to go back to the lattice gauge theory and expose the underlying mechanism that generates the modulation of the NSF when the temperature decreases and one enters the low-temperature quantum regime [25].

Notwithstanding the theoretical lines of inquiry above, there remain many open questions regarding the dynamics of spin ice materials [70]. Our results suggest that the use of polarized *inelastic* neutron scattering in such compounds could allow for the differentiation of the dynamics of the transverse and longitudinal modes [71]. In particular, the slow timescales of dynamics in classical spin ices at very low temperatures [70,72–74] may be accessible by applying polarization analysis to high-resolution backscattering or spin echo techniques [75], potentially yielding new insights into their dynamics in this regime.

We thank Cyrus Cerkauskas, Tom Fennell, and Jeffrey Rau for useful and stimulating discussions. This work was supported by the NSERC of Canada and the Canada Research Chair program (M. J. P. G., Tier 1). J. G. S. K. thanks Nanyang Technological University for financial support through the CN Yang Scholars Programme.

*Corresponding author.
ktchung@uwaterloo.ca

[1] O. Derzhko, J. Richter, and M. Maksymenko, Strongly correlated flat-band systems: The route from Heisenberg spins to Hubbard electrons, Int. J. Mod. Phys. B **29**, 1530007 (2015).

[2] D. Leykam, A. Andreanov, and S. Flach, Artificial flat band systems: from lattice models to experiments, Adv. Phys. **3**, 1473052 (2018).

[3] T. Mizoguchi and M. Udagawa, Flat-band engineering in tight-binding models: Beyond the nearest-neighbor hopping, Phys. Rev. B **99**, 235118 (2019).

[4] S. T. Bramwell and M. J. P. Gingras, Spin ice state in frustrated magnetic pyrochlore materials, Science **294**, 1495 (2001).

[5] M. Udagawa and L. Jaubert, *Spin Ice* (Springer-Verlag, Berlin, 2021).

[6] M. Höppner, S. Seiro, A. Chikina, A. Fedorov, M. Güttler, S. Danzenbächer, A. Generalov, K. Kummer, S. Patil, S. L. Molodtsov, Y. Kucherenko, C. Geibel, V. N. Strocov, M. Shi, M. Radovic, T. Schmitt, C. Laubschat, and D. V. Vyalikh, Interplay of Dirac fermions and heavy quasiparticles in solids, Nat. Commun. **4**, 1646 (2013).

[7] D. Marchenko, D. V. Evtushinsky, E. Golias, A. Varykhalov, T. Seyller, and O. Rader, Extremely flat band in bilayer graphene, Sci. Adv. **4**, eaau0059 (2018).

[8] W. Li, L. Chen, Z. Chen, Y. Hu, Z. Zhang, and Z. Liang, Probing the flat band of optically trapped spin-orbital-coupled Bose gases using Bragg spectroscopy, Phys. Rev. A **91**, 023629 (2015).

[9] S. Petit, E. Lhotel, B. Canals, M. C. Hatnean, J. Ollivier, H. Mutka, E. Ressouche, A. Wildes, M. Lees, and G. Balakrishnan, Observation of magnetic fragmentation in spin ice, Nat. Phys. **12**, 746 (2016).

[10] O. Benton, Quantum origins of moment fragmentation in $NdZr_2O_7$, Phys. Rev. B **94**, 104430 (2016).

[11] R. M. Moon, T. Riste, and W. C. Koehler, Polarization analysis of thermal-neutron scattering, Phys. Rev. **181**, 920 (1969).

[12] S. W. Lovesey, *Theory of Neutron Scattering from Condensed Matter* (Oxford University Press, New York, 1984), Vol. 2.

[13] M. J. P. Gingras and B. C. den Hertog, Origin of spin-ice behavior in Ising pyrochlore magnets with long-range dipole interactions: an insight from mean-field theory, Can. J. Phys. **79**, 1339 (2001).

[14] S. V. Isakov, R. Moessner, and S. L. Sondhi, Why Spin Ice Obeys the Ice Rules, Phys. Rev. Lett. **95**, 217201 (2005).

[15] C. L. Henley, Power-law spin correlations in pyrochlore antiferromagnets, Phys. Rev. B **71**, 014424 (2005).

[16] C. L. Henley, The "Coulomb Phase" in frustrated systems, Annu. Rev. Condens. Matter Phys. **1**, 179 (2010).

[17] C. Castelnovo, R. Moessner, and S. L. Sondhi, Spin ice, fractionalization, and topological order, Annu. Rev. Condens. Matter Phys. **3**, 35 (2012).

[18] T. Fennell, P. P. Deen, A. R. Wildes, K. Schmalzl, D. Prabhakaran, A. T. Boothroyd, R. J. Aldus, D. F. McMorrow, and S. T. Bramwell, Magnetic Coulomb phase in the spin ice $Ho_2Ti_2O_7$, Science **326**, 415 (2009).

[19] M. J. Harris, S. T. Bramwell, D. F. McMorrow, T. Zeiske, and K. W. Godfrey, Geometrical Frustration in the Ferromagnetic Pyrochlore $Ho_2Ti_2O_7$, Phys. Rev. Lett. **79**, 2554 (1997).

[20] S. T. Bramwell, M. J. Harris, B. C. den Hertog, M. J. P. Gingras, J. S. Gardner, D. F. McMorrow, A. R. Wildes, A. Cornelius, J. D. M. Champion, R. G. Melko, and T. Fennell, Spin Correlations in $Ho_2Ti_2O_7$: A Dipolar Spin Ice System, Phys. Rev. Lett. **87**, 047205 (2001).

[21] J. P. Clancy, J. P. C. Ruff, S. R. Dunsiger, Y. Zhao, H. A. Dabkowska, J. S. Gardner, Y. Qiu, J. R. D. Copley, T. Jenkins, and B. D. Gaulin, Revisiting static and dynamic spin-ice correlations in $Ho_2Ti_2O_7$ with neutron scattering, Phys. Rev. B **79**, 014408 (2009).

[22] P. H. Conlon and J. T. Chalker, Absent pinch points and emergent clusters: Further neighbor interactions in the pyrochlore Heisenberg antiferromagnet, Phys. Rev. B **81**, 224413 (2010).

[23] F. Flicker, *Magnetic Monopoles in Spin Ice*, Perimeter Scholar International Essay (Perimeter Institute for Theoretical Physics Waterloo, 2011).

[24] O. Benton, L. D. C. Jaubert, H. Yan, and N. Shannon, A spin-liquid with pinch-line singularities on the pyrochlore lattice, Nat. Commun. **7**, 11572 EP (2016).

[25] Y. Kato and S. Onoda, Numerical Evidence of Quantum Melting of Spin Ice: Quantum-to-Classical Crossover, Phys. Rev. Lett. **115**, 077202 (2015).

[26] M. Taillefumier, O. Benton, H. Yan, L. D. C. Jaubert, and N. Shannon, Competing Spin Liquids and Hidden Spin-Nematic Order in Spin Ice with Frustrated Transverse Exchange, Phys. Rev. X **7**, 041057 (2017).

[27] C. Castelnovo and R. Moessner, Rod motifs in neutron scattering in spin ice, Phys. Rev. B **99**, 121102(R) (2019).

[28] P. W. Anderson, Ordering and antiferromagnetism in ferrites, Phys. Rev. **102**, 1008 (1956).

[29] S. V. Isakov, K. Gregor, R. Moessner, and S. L. Sondhi, Dipolar Spin Correlations in Classical Pyrochlore Magnets, Phys. Rev. Lett. **93**, 167204 (2004).

[30] M. J. P. Gingras, Spin ice, in *Introduction to Frustrated Magnetism*, edited by C. Lacroix, P. Mendel, and F. Mila (Springer, New York, 2011), pp. 293–329.

[31] M. J. P. Gingras and P. A. McClarty, Quantum spin ice: a search for gapless quantum spin liquids in pyrochlore magnets, Rep. Prog. Phys. **77**, 056501 (2014).

[32] J. G. Rau and M. J. P. Gingras, Spin slush in an extended spin ice model, Nat. Commun. **7**, 12234 (2016).

[33] M. Udagawa, L. D. C. Jaubert, C. Castelnovo, and R. Moessner, Out-of-equilibrium dynamics and extended textures of topological defects in spin ice, Phys. Rev. B **94**, 104416 (2016).

[34] L. J. Chang, Y. Su, Y.-J. Kao, Y. Z. Chou, R. Mittal, H. Schneider, T. Brückel, G. Balakrishnan, and M. R. Lees, Magnetic correlations in the spin ice $Ho_{2-x}Y_xTi_2O_7$ as revealed by neutron polarization analysis, Phys. Rev. B **82**, 172403 (2010).

[35] See Supplemental Material at http://link.aps.org/supplemental/10.1103/PhysRevLett.128.107201 for conventions, analytical derivations, and supplemental figures. It also includes Refs. [36–41].

[36] H. E. Stanley, Spherical model as the limit of infinite spin dimensionality, Phys. Rev. **176**, 718 (1968).

[37] T. H. Berlin and M. Kac, The spherical model of a ferromagnet, Phys. Rev. **86**, 821 (1952).

[38] B. C. den Hertog and M. J. P. Gingras, Dipolar Interactions and Origin of Spin Ice in Ising Pyrochlore Magnets, Phys. Rev. Lett. **84**, 3430 (2000).

[39] R. G. Melko and M. J. P. Gingras, Monte Carlo studies of the dipolar spin ice model, J. Phys. Condens. Matter **16**, R1277 (2004).

[40] R. G. Melko, B. C. den Hertog, and M. J. P. Gingras, Long-Range Order at Low Temperatures in Dipolar Spin Ice, Phys. Rev. Lett. **87**, 067203 (2001).

[41] M. R. Luo, in *Encyclopedia of Color Science and Technology* (Springer, Berlin Heidelberg, 2015), pp. 1–7.

[42] Quantum (non-Ising) exchange terms are expected to be very small in the extensively studied (effectively classical) $Ho_2M_2O_7$ and $Dy_2M_2O_7$ (M = Ti, Sn and Ge) spin ice materials [43].

[43] J. G. Rau and M. J. P. Gingras, Magnitude of quantum effects in classical spin ices, Phys. Rev. B **92**, 144417 (2015).

[44] A. S. Wills, M. E. Zhitomirsky, B. Canals, J. P. Sanchez, P. Bonville, P. D. de Réotier, and A. Yaouanc, Magnetic ordering in $Gd_2Sn_2O_7$: the archetypal Heisenberg pyrochlore antiferromagnet, J. Phys. Condens. Matter **18**, L37 (2006).

[45] A. Del Maestro and M. J. P. Gingras, Low-temperature specific heat and possible gap to magnetic excitations in the Heisenberg pyrochlore antiferromagnet $Gd_2Sn_2O_7$, Phys. Rev. B **76**, 064418 (2007).

[46] A. P. Ramirez, A. Hayashi, R. J. Cava, R. Siddharthan, and B. S. Shastry, Zero-point entropy in 'spin ice', Nature (London) **399**, 333 (1999).

[47] L.-J. Chang, S. Onoda, Y. Su, Y.-J. Kao, K.-D. Tsuei, Y. Yasui, K. Kakurai, and M. R. Lees, Higgs transition from a magnetic Coulomb liquid to a ferromagnet in $Yb_2Ti_2O_7$, Nat. Commun. **3**, 992 (2012).

[48] D. A. Garanin, The $1/D$ expansion for classical magnets: Low-dimensional models with magnetic field, J. Stat. Phys. **83**, 907 (1996).

[49] B. Canals and D. A. Garanin, Spin-liquid phase in the pyrochlore anti-ferromagnet, Can. J. Phys. **79**, 1323 (2001).

[50] T. Mizoguchi, L. D. C. Jaubert, R. Moessner, and M. Udagawa, Magnetic clustering, half-moons, and shadow pinch points as signals of a proximate Coulomb phase in frustrated Heisenberg magnets, Phys. Rev. B **98**, 144446 (2018).

[51] É. Lantagne-Hurtubise, J. G. Rau, and M. J. P. Gingras, Spin-Ice Thin Films: Large-N Theory and Monte Carlo Simulations, Phys. Rev. X **8**, 021053 (2018).

[52] In the Supplemental Material [35], we show that the ferromagnetic $J_1 < 0$ model also exhibits a flat (hhl) NSF in its paramagnetic phase.

[53] J. N. Reimers, A. J. Berlinsky, and A.-C. Shi, Mean-field approach to magnetic ordering in highly frustrated pyrochlores, Phys. Rev. B **43**, 865 (1991).

[54] J. P. C. Ruff, R. G. Melko, and M. J. P. Gingras, Finite-Temperature Transitions in Dipolar Spin Ice in a Large Magnetic Field, Phys. Rev. Lett. **95**, 097202 (2005).

[55] Z. Hiroi, K. Matsuhira, and M. Ogata, Ferromagnetic Ising spin chains emerging from the spin ice under magnetic field, J. Phys. Soc. Jpn. **72**, 3045 (2003).

[56] R. Higashinaka and Y. Maeno, Field-Induced Transition on a Triangular Plane in the Spin-Ice Compound $Dy_2Ti_2O_7$, Phys. Rev. Lett. **95**, 237208 (2005).

[57] P. A. McClarty, O. Sikora, R. Moessner, K. Penc, F. Pollmann, and N. Shannon, Chain-based order and quantum spin liquids in dipolar spin ice, Phys. Rev. B **92**, 094418 (2015).

[58] D. L. Bergman, C. Wu, and L. Balents, Band touching from real-space topology in frustrated hopping models, Phys. Rev. B **78**, 125104 (2008).

[59] A. B. Harris, C. Kallin, and A. J. Berlinsky, Possible néel orderings of the kagomé antiferromagnet, Phys. Rev. B **45**, 2899 (1992).

[60] S. Onoda and Y. Tanaka, Quantum fluctuations in the effective pseudospin-$\frac{1}{2}$ model for magnetic pyrochlore oxides, Phys. Rev. B **83**, 094411 (2011).

[61] J. G. Rau and M. J. P. Gingras, Frustrated quantum rare-earth pyrochlores, Annu. Rev. Condens. Matter Phys. **10**, 357 (2019).

[62] P. Henelius, T. Lin, M. Enjalran, Z. Hao, J. G. Rau, J. Altosaar, F. Flicker, T. Yavors'kii, and M. J. P. Gingras, Refrustration and competing orders in the prototypical $Dy_2Ti_2O_7$ spin ice material, Phys. Rev. B **93**, 024402 (2016).

[63] R. A. Borzi, F. A. Gomez Albarracin, H. D. Rosales, G. L. Rossini, A. Steppke, D. Prabhakaran, A. P. Mackenzie, D. C. Cabra, and S. A. Grigera, Intermediate magnetization state and competing orders in $Dy_2Ti_2O_7$ and $Ho_2Ti_2O_7$, Nat. Commun. **7**, 12592 (2016).

[64] C. Castelnovo, R. Moessner, and S. L. Sondhi, Magnetic monopoles in spin ice, Nature (London) **451**, 42 (2008).

[65] L. Pili, A. Steppke, M. E. Barber, F. Jerzembeck, C. W. Hicks, P. C. Guruciaga, D. Prabhakaran, R. Moessner, A. P. Mackenzie, S. A. Grigera, and R. A. Borzi, Dynamics and thermodynamics of a topological transition in spin ice materials under strain, arXiv:2105.07977.

[66] T. Lin, X. Ke, M. Thesberg, P. Schiffer, R. G. Melko, and M. J. P. Gingras, Nonmonotonic residual entropy in diluted spin ice: A comparison between monte carlo simulations of diluted dipolar spin ice models and experimental results, Phys. Rev. B **90**, 214433 (2014).

[67] R. J. Aldus, T. Fennell, P. P. Deen, E. Ressouche, G. C. Lau, R. J. Cava, and S. T. Bramwell, Ice rule correlations in stuffed spin ice, New J. Phys. **15**, 013022 (2013).

[68] M. Hermele, M. P. A. Fisher, and L. Balents, Pyrochlore photons: The $U(1)$ spin liquid in a $S = \frac{1}{2}$ three-dimensional frustrated magnet, Phys. Rev. B **69**, 064404 (2004).

[69] O. Benton, O. Sikora, and N. Shannon, Seeing the light: Experimental signatures of emergent electromagnetism in a quantum spin ice, Phys. Rev. B **86**, 075154 (2012).

[70] K. Matsuhira, Dynamics, in *Spin Ice*, edited by M. Udagawa and L. Jaubert (Springer-Verlag, Berlin, 2021), pp. 71–91.

[71] M. I. Ryzhkin, I. A. Ryzhkin, and S. T. Bramwell, Dynamic susceptibility and dynamic correlations in spin ice, Europhys. Lett. **104**, 37005 (2013).

[72] A. M. Samarakoon, S. A. Grigera, D. A. Tennant, A. Kirste, B. Klemke, P. Strehlow, M. Meissner, J. N. Hallen, L. Jaubert, C. Castelnovo, and R. Moessner, Anomalous magnetic noise in imperfect flat bands in the topological magnet $Dy_2Ti_2O_7$, arXiv:2107.11379.

[73] B. Tomasello, C. Castelnovo, R. Moessner, and J. Quintanilla, Correlated Quantum Tunneling of Monopoles in Spin Ice, Phys. Rev. Lett. **123**, 067204 (2019).

[74] L. D. C. Jaubert and P. C. W. Holdsworth, Magnetic monopole dynamics in spin ice, J. Phys. Condens. Matter **23**, 164222 (2011).

[75] J. S. Gardner, G. Ehlers, A. Faraone, and V. G. Sakai, High-resolution neutron spectroscopy using backscattering and neutron spin-echo spectrometers in soft and hard condensed matter, Nat. Rev. Phys. **2**, 103 (2020).